Comparative Analysis of $MgCl_2$ (Salt PCM) and Aluminum (Metallic PCM) for Melting and Solidification Performance in Latent Heat Storage

IOP Conf. Series: Earth and Environmental Science **1588** (2026) 012007 doi:10.1088/1755-1315/1588/1/012007

Comparative Analysis of $MgCl_2$ (Salt PCM) and Aluminum (Metallic PCM) for Melting and Solidification Performance in Latent Heat Storage

İsmail Gürkan Demirkıran[1,2*], Klarissa Niedermeier[2] and Erdal Cetkin[1]

[1] Department of Mechanical Engineering, İzmir Institute of Technology, İzmir, Türkiye
[2] Institute for Thermal Energy Technology and Safety, Karlsruhe Institute of Technology, Karlsruhe, Germany

[*]E-mail: ismaildemirkiran@iyte.edu.tr

Abstract. Next-generation concentrated solar power systems require thermal energy storage technologies capable of reliable operation above 600 °C. This study numerically compares aluminum as a metallic phase change material (PCM) and $MgCl_2$ as a salt PCM (enhanced with perforated fins) in a shell-and-tube TES unit using liquid sodium as the heat transfer fluid. Simulations were carried out with the enthalpy–porosity method in ANSYS Fluent 2024R2. Contrary to assumptions in the literature, natural convection is not negligible during melting or solidification of aluminum, underlining the need to account for convection in metallic PCM modeling. Results further show that for aluminum, melting and solidification times are almost identical, with only a 7-minute difference, and the overall phase change is nearly twice as fast as $MgCl_2$. Moreover, the obtained outlet temperature profiles ensure suitable operating conditions for turbines, while the nearly constant heat flux trend approximates steady-state system behavior.

1. Introduction

One of the major advancements in renewable energy is the pursuit of higher efficiency in concentrated solar power (CSP) plants. Increasing the operating temperature enhances thermodynamic performance and lowers the levelized cost of energy. To achieve broader decarbonization targets, the integration of thermal energy storage (TES) is essential, as it stabilizes supply and demand and enables continuous 24/7 operation [1].

Compared to electrochemical or hydrogen-based systems, TES provides significant advantages in large-scale applications due to its lower cost and design flexibility. In CSP plants, TES improves the capacity factor while reducing both electricity and storage costs. However, most existing systems rely on single- or two-tank sensible heat storage, which are prone to thermal fluctuations during charging and discharging. Different TES technologies exhibit trade-offs between power and energy density [2]. Hybrid concepts that combine sensible and latent TES can mitigate these limitations, offering improved overall system performance [3]. The missing key requirement, however, is that the outlet temperature of the storage unit remains within the operational range of CSP components, including steam or gas turbines and the solar receiver.

This study addresses the challenges in next-generation CSP systems designed to operate above 600 °C, where only a limited number of fluids and structural materials remain thermally and chemically stable. Liquid metals (LMs) have emerged as promising heat transfer fluids (HTFs)

and metallic phase change materials (PCMs) for thermal storage, owing to their high thermal conductivity, stability, and resistance to decomposition at elevated temperatures. These properties also make them attractive for high-temperature industrial sectors such as metallurgy and ceramics. By contrast, in the same temperature range, various molten-salt-based PCMs exhibit superior latent heat storage capacity and specific heat values compared to metals, but their thermal conductivities are significantly lower[1].

Molten salt PCMs suffer from inherently low thermal conductivity, and numerous studies have therefore focused on enhancing their heat transfer performance. In contrast, with recent advances in material compatibility, mechanical strength, and corrosion resistance between structural materials and molten metals, metallic PCMs have emerged as promising alternatives. Unlike molten salts, metallic PCMs do not require additional strategies to improve thermal conductivity, making them particularly attractive for high-temperature applications [4]. Li et al. [5] compared two high-temperature composite PCMs: aluminum and $NaLiCO_3$, using alumina and MgO as the respective supporting structural materials. Their findings demonstrate that the aluminum composite delivers superior thermal performance, exhibiting more than twice the thermal conductivity of the salt composite while maintaining a comparable thermal energy storage density. To prevent leakage, corrosion, and oxidation of aluminum, various researchers [6–8] have investigated different encapsulation techniques and materials at both micro- and macro-scales. Zhao et al. [9] successfully demonstrated 3000 phase change cycles—equivalent to approximately eight years of operation in CSP plants—using macrocapsules with an aluminum core encapsulated by alumina and an additional inner cavity. The process was conducted safely and without significant changes in the thermophysical properties of the PCM. The shell diameter was scaled up to 31.5 mm, which preserved the latent storage capacity by enabling a higher core-to-shell diameter ratio.

Phase change behavior and thermal enhancement of $MgCl_2$ using graphite porous foams have been studied experimentally and numerically many times before [10–13]. In addition, our recent work demonstrated that the overall thermal conductivity of $MgCl_2$ can be improved within a shell-and-tube heat exchanger by employing innovative fin designs, thereby increasing its applicability for CSP applications [14]. However, few studies attempt to evaluate melting and solidification performances of metallic PCMs. Alemam et al. [15] experimentally investigated the phase-change cycling performance (5–8 h charging and 10–15 h discharging) of a power-to-power high-temperature storage unit employing liquid sodium as the HTF and Al–Si as the metallic PCM in a truncated cone-shaped tank with a large diameter of 1.63 m. The system responded in under 5 minutes to changes in the demanded discharge power, reflecting the fast charge/discharge behaviour of the metallic PCM. Furthermore, the high thermal conductivity of Al–Si enabled the discharging process to continue through sensible heat release even after the solidification phase was completed. In another study, Alemam et al. simulated the solidification process of Al–Si using the same geometric dimensions of the PCM tank. In the convection-neglected CFD analysis considering high heat diffusion capability of Al-Si, the predicted temperature evolution deviated by less than 5 °C from the experimental data. Previously, Kotze et al. [16] also neglected natural convection for the solidification process of Al-Si in a shell-and-tube storage unit. Yang et al. [17] numerically compares melting behaviours of eicosane as paraffin PCM and gallium as metallic PCM in a vertical heated cavity. The results indicate that although liquid gallium exhibits much stronger natural convection than eicosane, it contributes little to overall heat transfer because gallium's thermal conductivity is over 200 times higher. In contrast, the weak conductivity of eicosane makes convection a dominant mechanism, whereas in gallium, conduction is so effective

that convective heat transfer remains comparatively insignificant despite the more vigorous flow. Shan et al. [18] aims to reduce the outlet temperatures of latent heat storage units appropriate to the operation condition of the CSP receiver and the steam generator during charging and discharging processes, respectively. For this purpose, they select two different high temperature metallic PCMs in spherical encapsulation pellets, which are Al-Si (T_m=577 °C) and Al-Si-Cu (T_m=577 °C), and use NaOH as heat transfer fluid (HTF). Under identical CSP operating conditions, the single PCM case with Al-Si-Cu causes lower HTF outlet temperatures in average than with Al-Si and cascaded configurations.

The present study aims to comparatively evaluate the melting and solidification behaviour of aluminum as a metallic PCM in a horizontally arranged shell-and-tube storage tank, employing liquid sodium as the HTF. Its thermal performance is benchmarked against that of $MgCl_2$, a molten salt PCM, whose effective conductivity is enhanced through innovative fin designs within the same configuration. By focusing on the evolution of heat flux and outlet temperature profiles, the study highlights the distinct thermal transport mechanisms of metallic versus molten-salt PCMs, thereby providing insights into their suitability for next-generation high-temperature TES systems in CSP applications.

2. Numerical Model

2.1 Physical domain and thermophysical properties

Figure 1 depicts the shell-and-tube TES unit, in which the high-temperature HTF, heated by the CSP receiver, flows through the inner tube, while the PCM fills the annular space between the shell and the HTF pipe. The primary role of this latent heat storage system is to absorb thermal energy from the HTF, thereby lowering its temperature before returning it to the CSP receiver during

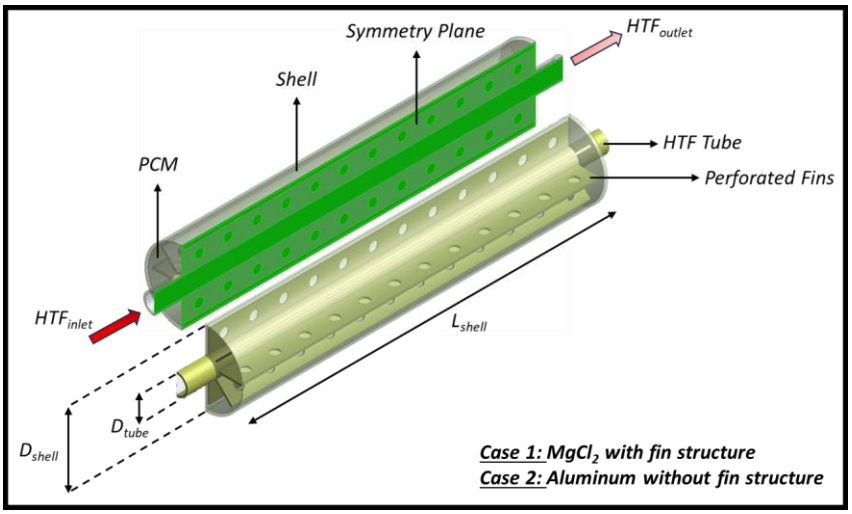

Figure 1. Schematic of a shell-and-tube heat exchanger filled with PCM [14].

charging, and to supply heat within the suitable temperature range for steam or gas turbine operation during discharging. To enhance heat transfer when employing low-conductivity molten salt PCMs such as $MgCl_2$, the tubes are equipped with innovative fin structures, as demonstrated in [14]. In contrast, when aluminum is used as a metallic PCM in the current study, no additional

heat transfer enhancement is required. Furthermore, the horizontal configuration provides advantages such as lower thermal stresses and enhanced structural stability compared with vertical designs [19]. In current study, a concentrically centered tube was adopted to simplify the geometry and to focus primarily on evaluating the influence of fin modifications.

All geometric dimensions are listed in Table 1, while the details of the fin structure for the $MgCl_2$ case (Case 1) are provided in our previous work [14]. Owing to the volume occupied by the

Table 1. General dimensions of Heat Exchanger (HEX)

HEX Geometry	
D_{tube_inner} [mm]	30
D_{tube_outer} [mm]	36
D_{shell_inner} [mm]	120
D_{shell_outer} [mm]	126
D_{shell}/D_{tube}	3
L_{shell} [mm]	600

extended fins, the storage capacities of $MgCl_2$ and aluminum differ; however, this disparity is not critical, as their latent heat capacities are inherently distinct. The primary objective of this study is to compare the charging and discharging times, the evolution of liquid fraction, heat flux, and outlet temperature profiles.

Next-generation CSP systems may operate at up to 1000 °C [37], where conventional fluids and materials fail due to corrosion, phase separation, and durability issues. Liquid sodium is

Table 2. Thermophysical properties of Liquid Na as HTF, Inconel Alloy 617 as structural material, $MgCl_2$ as salt PCM and Aluminum as metallic PCM.

	Latent heat of fusion (kJ/kg)	Melting point (°C)	Density (kg/m^3)	Thermal Conductivity (W/mK)	Specific heat (J/kgK)	Dynamic viscosity (Pas)
Liquid Na	-	-	$966.74-0.1274874\ T-5.38*10^{-5}\ T^2$	$98.91-0.046\ T-3.714x10^{-6}\ T^2$	1380	$0.103\ T^{-0.9103}$
Inconel alloy 617	-	-	8360	24.2	586	-
$MgCl_2$	452	714	2320 (at 25°C), 1680 (at 714°C)	0.46 (at 714°C)	$0.7602+1.6567\ 10^{-4}*T$ (absolute temp.)	0.0032
Aluminum	397	660	2375	204	0.89	0.0013

selected as the HTF, as it offers high thermal conductivity, low density, and cost-effectiveness compared with other liquid metals [20]. Thermophysical properties of liquid sodium [21] (as HTF), Inconel alloy 617 [11] (as structural material for tube and shell domains), $MgCl_2$ [13] (as salt PCM) and Aluminum[2] (as metallic PCM) are listed in Table 2, where temperature variable is given in Kelvin unit.

2.2 Governing equations, assumptions and boundary conditions

Transient heat transfer from the HTF to the PCM cavity, fluid flow inside the tube, buoyancy-driven convection, and PCM melting/solidification are simulated in a 3D computational domain using ANSYS 2024R2. The enthalpy–porosity method is applied to implicitly track the solid–liquid interface, accounting for buoyancy forces and enthalpy equilibrium during phase change. To simplify the computations, the following assumptions are adopted: (i) both HTF flow and liquid PCM circulation are unsteady and laminar; (ii) buoyancy effects from density variations in melted PCM are included and modeled with the Boussinesq approximation; (iii) phase change occurs under isothermal conditions; and (iv) radiation, viscous dissipation, and volumetric expansion of PCM are neglected.

Radiative heat transfer gains importance at elevated operating temperatures due to the ability of PCMs to emit and absorb radiation. However, Shen et al. [22] showed that when fins are uniformly distributed within the PCM, conduction dominates the heat transfer process and the contribution of radiation becomes weak in high-conductivity systems. Consequently, when aluminum or other metallic PCMs are employed, their inherently high thermal conductivity allows the phase change process to be modeled in a similar manner, with radiative heat transfer reasonably neglected.

The HTF flow is set to the laminar regime with a Reynolds number of Re = 1000. From the perspective of melted PCM flow dynamics, a common approach is to use either the HTF tube diameter or the PCM thickness between the shell and tube as the characteristic length for horizontally oriented systems, whereas the HTF tube length is typically used as the characteristic length in vertical orientations. Owing to the relatively small characteristic length scales associated with the tube diameter or PCM thickness, the flow regime does not transition to turbulence, which represents realistic operating conditions [21]. Therefore, turbulent effects are neglected in the phase change model.

With these assumptions and activation of the 'Solidification/Melting Module,' the conservation equations of mass, momentum, and energy are solved for the 3D domain, as expressed in Eqs. (1–4).

Mass equation:

$$\frac{\partial \rho}{\partial t} + \nabla(\rho \mathbf{u}) = 0 \tag{1}$$

Momentum equation in x-direction:

$$\frac{\partial(\rho u)}{\partial t} + \nabla \cdot (\rho \boldsymbol{u} u) = \nabla \cdot (\mu \nabla \mathrm{u}) - \frac{\partial P}{\partial x} + Au \tag{2}$$

Momentum equation in y-direction:

$$\frac{\partial(\rho v)}{\partial t} + \nabla \cdot (\rho \boldsymbol{u} v) = \nabla \cdot (\mu \nabla \mathrm{v}) - \frac{\partial P}{\partial y} + Av + S_{buoyancy} \tag{3}$$

Momentum equation in z-direction:

$$\frac{\partial(\rho w)}{\partial t}+\nabla\cdot(\rho \boldsymbol{u}\boldsymbol{w})=\nabla\cdot(\mu\ \nabla\ \mathrm{w})-\frac{\partial P}{\partial z}+Aw \tag{4}$$

The velocity vector **u** consists of the components *u*, *v*, and *w* in the *x*, *y*, and *z* directions, respectively. ρ and μ denote the material density and dynamic viscosity, while *P* and *T* represent pressure and temperature. In the melted PCM, temperature variations induce density gradients that, combined with gravity, generate buoyancy forces driving upward or downward fluid motion, as described in Eq. (5).

$$S_{buoyancy}=\rho_{ref}g\beta(T-T_{ref}) \tag{5}$$

Here, *g* and *β* denote gravitational acceleration and the thermal expansion coefficient. Unlike the standard Navier–Stokes equations, a porosity function *A* is added to dissipate momentum during solidification. In Eq. (6), the liquid fraction *lf* represents the Carman–Kozeny porosity term, which vanishes at full solidification, enforcing momentum dissipation. A small constant *b* prevents division by zero, while the mushy zone constant (10^5 kg/(m^3·s) in Fluent) governs interface morphology and phase change progression.

$$A=-C\frac{(1-lf)^2}{lf^3+b} \tag{6}$$

The energy equation is expressed in terms of enthalpy rather than temperature, as it simultaneously accounts for sensible and latent heat storage. Heat transfer first leads to a temperature increase in the solid or liquid PCM, and second to a solid–liquid phase change, during which the temperature remains nearly constant despite ongoing heat exchange. As shown in Eq. (7), these processes are represented by sensible and latent enthalpy contributions, respectively.

$$\frac{\partial(\rho h_{sens})}{\partial t}+\nabla\cdot(\rho \boldsymbol{u}h_{sens})=\nabla\cdot(k\ \nabla T)+S_{ph} \tag{7}$$

The energy source term S_{ph} (Eq. (8)) is introduced to capture the melting/solidification dynamics once the PCM reaches its phase change temperature.

$$S_{ph}=\frac{\partial(\rho\ \mathrm{h_{lat}})}{\partial t}+\nabla(\rho \boldsymbol{u}\ \mathrm{h_{lat}}) \tag{8}$$

The total enthalpy is obtained as the sum of sensible and latent heat contributions.

Heat absorption up to the solidus temperature increases sensible heat with a temperature rise. Between the solidus and liquidus temperatures (T_s and T_l), heat transfer drives melting while also adding to sensible storage. After complete melting, further heat input raises the PCM temperature and sensible heat content. Eq. (9) defines the enthalpy in terms of the instantaneous PCM temperature and the phase-change temperature range, shown here for the melting process.

$$h = \begin{cases} \int_{T_{initial}}^{T_s} c_p \, \mathrm{dT} & \text{if } \mathrm{T} < \mathrm{T}_s \\ \int_{T_s}^{T_l} c_p \, \mathrm{dT} + \mathrm{lf\,L} & \text{if } \mathrm{T}_s < \mathrm{T} < \mathrm{T}_l \\ \int_{T_l}^{T} c_p \, \mathrm{dT} & \text{if } \mathrm{T}_l < T \end{cases} \tag{9}$$

For both melting and solidification of each PCM, all subdomains are assumed to have a uniform initial temperature, with the difference from the PCM melting temperature set to $|T_{melting} - T_{initial}| = 24$ K. Heat transfer is driven by hot or cold HTF flowing inside the tube, interacting with the PCM through the tube and fins during melting and solidification, respectively. The inlet HTF temperature is defined such that $|T_{inlet} - T_{melting}| = 36$ K for both processes. Detailed initial and boundary conditions are provided in Table 3.

Table 3. Prescribed boundary and initial conditions of $MgCl_2$ and Aluminum for charging and discharging processes.

$MgCl_2$

Initial and Boundary Conditions for Melting (°C)		Initial and Boundary Conditions for Solidification (°C)	
$T_{initial}$	690	$T_{initial}$	738
$T_{melting}$	714	$T_{melting}$	714
T_{inlet}	750	T_{inlet}	678

Aluminum

Initial and Boundary Conditions for Melting (°C)		Initial and Boundary Conditions for Solidification (°C)	
$T_{initial}$	636	$T_{initial}$	684
$T_{melting}$	660	$T_{melting}$	660
T_{inlet}	696	T_{inlet}	624

Prior to the formal analysis, mesh and time-step independence of the numerical model were verified, and the model was validated against experimental data. Further details are available in our previous work [14].

3. Results and Discussions

3.1 Melting and solidification processes of $MgCl_2$

Figure 2 presents the melting and solidification performance of $MgCl_2$ thermally enhanced with perforated fin structures, evaluated in terms of liquid fraction and outlet temperature. Detailed liquid fraction contour plots can be found in [14]. As shown in Figure 2a, there is a significant difference between charging and discharging times. Both processes exhibit nearly linear trends; however, melting is completed in approximately 6 hours, whereas solidification extends beyond 7 hours. This discrepancy arises from the presence of natural convection during the melting of $MgCl_2$. Figure 2b illustrates the evolution of outlet temperatures, which differ markedly from the liquid fraction profiles. As listed in Table 3, liquid sodium enters the heat exchanger at 750 °C, 36 K above the melting temperature of $MgCl_2$. At the onset of melting, the HTF enters the tube at 750 °C, but its temperature drops to about 690 °C at the outlet due to the high heat-transfer rate resulting from the large temperature gradient. After this initial drop, the increase becomes more gradual as the molten PCM surrounding the finned tube forms an insulating layer.

During solidification, the HTF inlet temperature is set to 678 °C, maintaining the same 36 K difference relative to the PCM melting point. Similarly, the outlet temperature shows a sharp initial decrease. Unlike the melting case, however, no further change is observed in the subsequent stage of solidification. This contrast results from the weak influence of natural convection in solidification. Although the outlet temperatures vary almost uniformly, the system behaviour remains transient throughout the processes.

3.2 Melting and solidification processes of aluminum

Table 3 lists the initial temperatures of all components and the inlet temperatures of liquid

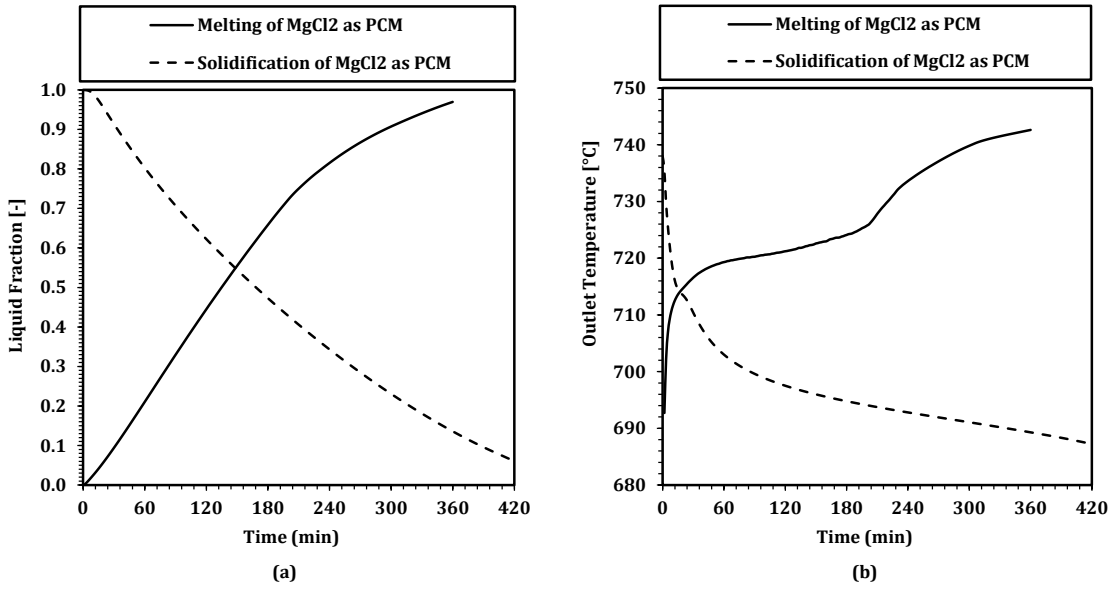

Figure 2. Variation of (a) liquid fraction, and (b) outlet temperature values during solidification process of $MgCl_2$ as PCM with perforated fins.

sodium for the melting and solidification of aluminum. The temperature differences were adjusted relative to the phase change temperature of aluminum, ensuring identical temperature gradients.

Figures 3a and 3b present the liquid fraction contours of aluminum during melting, shown in isometric and axial views, respectively. The results reveal the influence of natural convection on PCM distribution even at the early stages of charging. Circulations in the upper region of the tube accelerate melting, while the lower region exhibits a noticeable delay. Contrary to expectations based solely on the high thermal conductivity of aluminum, natural convection enhances melting predominantly in the upper region. This confirms the necessity of accounting for convection effects in the numerical modeling of metallic PCMs.

The axial view in Figure 3b provides an even more striking observation. Unlike what is commonly reported in the literature, melting does not initiate simultaneously along the entire tube surface. Instead, phase change first occurs near the inlet of the storage volume, while the remaining aluminum remains solid until the front region has nearly completed melting. This behavior arises from aluminum's exceptionally high thermal conductivity, which enables the storage unit to absorb large amounts of heat before melting propagates further downstream.

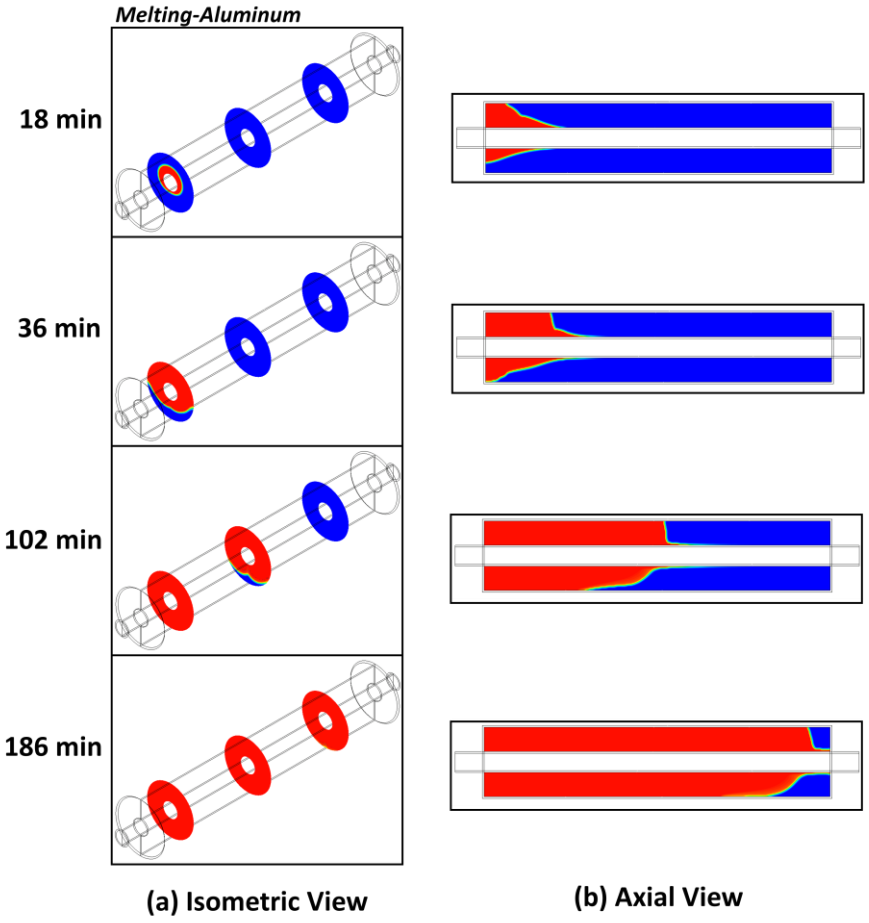

Figure 3. Contours of liquid fraction during melting process of aluminum as PCM without fins. Melting propagation in (a) isometric and (b) axial direction, respectively.

Similar trends are observed during the solidification of aluminum. Although previous studies suggest that natural convection can generally be neglected—due to its weak influence during solidification of various PCMs and the high thermal conductivity of metallic PCMs—the present results indicate otherwise. As shown in Figure 4a, solidification initiates more rapidly at the bottom of the tube, and this behaviour persists across subsequent time steps and downstream cross-sections. The axial contours in Figure 4b further confirm this effect. Midway through discharging, however, solidification becomes more uniform across the top and bottom regions. Consistent with the melting process, solidification does not commence in the downstream cross-section until the entrance region is nearly complete.

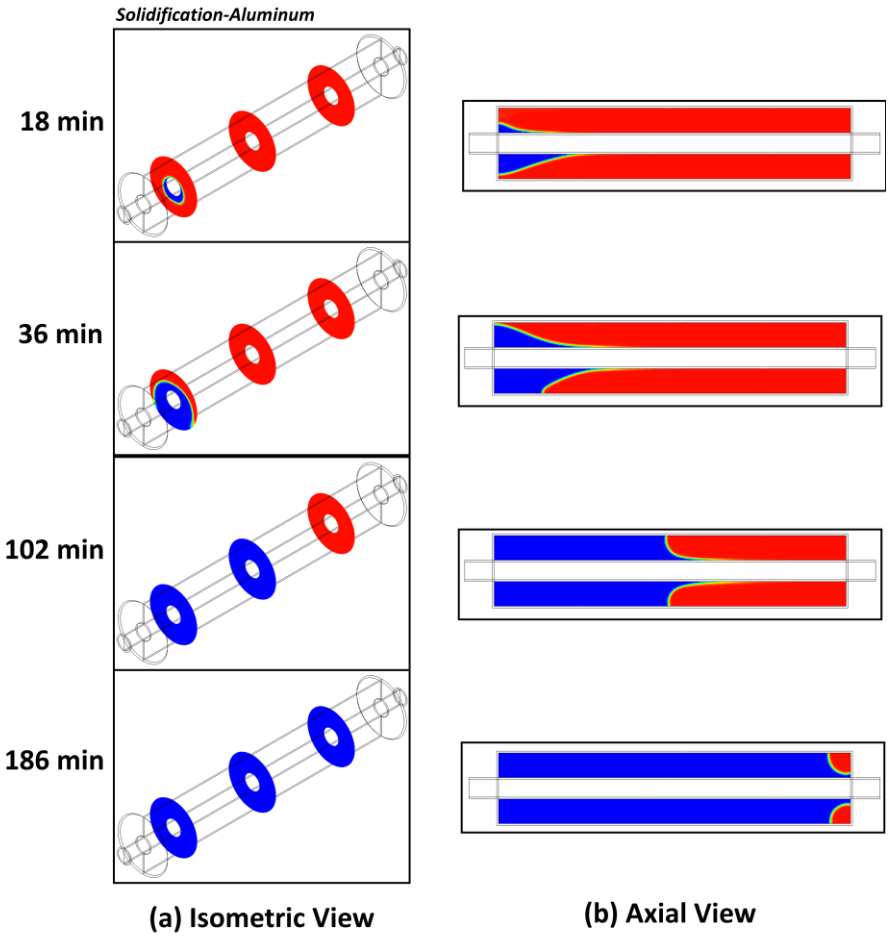

Figure 4. Contours of liquid fraction during solidification process of aluminum as PCM without fins. Melting propagation in (a) isometric and (b) axial direction, respectively.

Figure 5 further supports the observations from the liquid fraction results. For aluminum, both melting and solidification exhibit nearly linear evolution, with only a 7-minute difference

between the two processes (Figure 5a), compared to about 1 hour for $MgCl_2$. Moreover, the phase change processes are obviously faster, with solidification taking roughly half the time compared to $MgCl_2$. Heat flux values also show an almost perfect match, enabling flexible design of latent heat storage units for CSP regulation. Throughout most of the phase change duration, the heat flux remains nearly constant, approximating steady-state behaviour. Another key advantage of metallic PCMs is the stability of outlet temperatures during both melting and solidification, which is critical for maintaining steam and gas turbine operation within the required temperature range and for ensuring suitable inlet conditions at the CSP receiver.

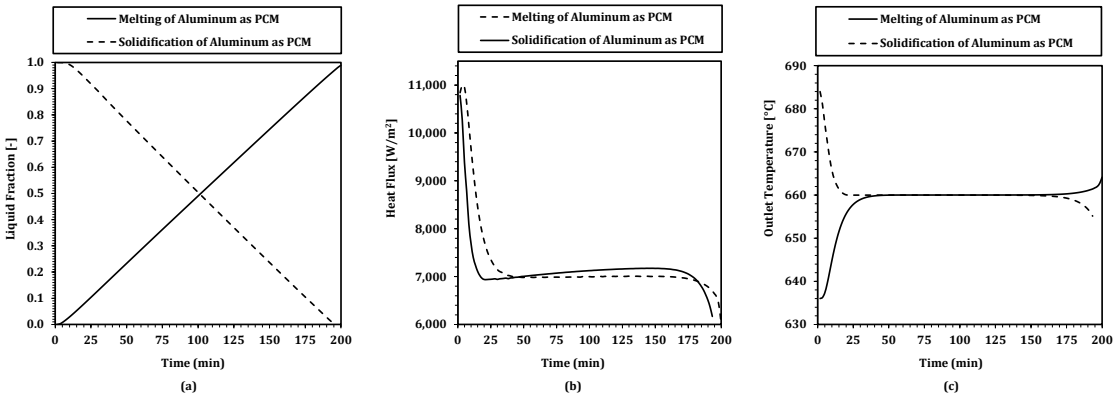

Figure 5. Transient variation in **(a)** liquid fraction, **(b)** heat flux, and **(c)** outlet temperature during melting and solidification processes of aluminum without fins.

Conclusions

A comparative numerical investigation of $MgCl_2$ and aluminum as PCMs in a shell-and-tube TES configuration was conducted to assess their suitability for high-temperature CSP systems. Key findings can be summarized as follows:

1. Natural convection: Contrary to common assumptions, convection significantly influences both melting and solidification of aluminum and must be considered in metallic PCM modeling.

2. Thermal stability: Aluminum shows nearly identical heat flux in charging and discharging, with stable outlet temperatures.

3. Operational benefits: Its steady thermal behavior supports consistent turbine inlet conditions and flexible TES operation.

4. $MgCl_2$ asymmetry: Melting proceeds faster than solidification, with about a one-hour time gap due to convection.

5. Aluminum's advantage: Phase change is nearly symmetric, with only a 7-minute difference and about half the total duration of $MgCl_2$. Increasing the storage volume of aluminum enables it to deliver a storage capacity equivalent to that of $MgCl_2$.

Overall, metallic PCMs such as aluminum offer faster response, stable thermal output, and superior integration potential compared to molten salts, without requiring additional heat transfer enhancement.

Acknowledgements

This work was supported by the European Union's Horizon 2020 research and innovation programme under grant agreement No. 101036910 (StoRIES project). Numerical simulations were performed on the bWUniCluster high-performance computing system at the Karlsruhe Institute of Technology (KIT), Baden-Württemberg, Germany.

References

[1] T. Ong *et al.*, "Review on the challenges of salt phase change materials for energy storage in concentrated solar power facilities," *Appl. Therm. Eng.*, vol. 238, no. October 2023, p. 122034, 2024, doi: 10.1016/j.applthermaleng.2023.122034.

[2] D. S. Jayathunga, H. P. Karunathilake, M. Narayana, and S. Witharana, "Phase change material (PCM) candidates for latent heat thermal energy storage (LHTES) in concentrated solar power (CSP) based thermal applications - A review," *Renew. Sustain. Energy Rev.*, vol. 189, no. PB, p. 113904, 2024, doi: 10.1016/j.rser.2023.113904.

[3] A. Alemam, S. N. Gunasekara, J. N. W. Chiu, K. Niedermeier, and I. Afgan, "Investigation of hybrid sensible-latent packed bed thermal energy storage system," *Appl. Therm. Eng.*, vol. 279, no. PA, p. 127375, 2025, doi: 10.1016/j.applthermaleng.2025.127375.

[4] M. Imran Khan, F. Asfand, and S. G. Al-Ghamdi, "Progress in research and development of phase change materials for thermal energy storage in concentrated solar power," *Appl. Therm. Eng.*, vol. 219, no. PB, p. 119546, 2023, doi: 10.1016/j.applthermaleng.2022.119546.

[5] Q. Li *et al.*, "Fabrication and thermal properties investigation of aluminium based composite phase change material for medium and high temperature thermal energy storage," *Sol. Energy Mater. Sol. Cells*, vol. 211, no. December 2019, 2020, doi: 10.1016/j.solmat.2020.110511.

[6] B. Zhao, X. Jiang, D. Liu, H. Guo, N. Sheng, and C. Zhu, "Hybridized Al metal phase change & CaCO3 thermochemical energy storage for high-temperature heat storage," *Chem. Eng. J.*, vol. 519, no. May, p. 165587, 2025, doi: 10.1016/j.cej.2025.165587.

[7] J. Z. Benner, R. C. Shannon, W. Wu, L. Shen, A. P. Metsack, and J. Zhao, "The effect of micro-encapsulation on thermal characteristics of metallic phase change materials," *Appl. Therm. Eng.*, vol. 207, no. December 2021, p. 118055, 2022, doi: 10.1016/j.applthermaleng.2022.118055.

[8] Y. Wang, S. Li, D. Zou, N. Sheng, and C. Zhu, "Multifunctional SrFeO3-δ@Al composite macrocapsules for synergistic high-temperature thermal storage and oxygen separation," *Chem. Eng. J.*, vol. 520, no. March, p. 166053, 2025, doi: 10.1016/j.cej.2025.166053.

[9] B. Zhao *et al.*, "Development of over 3000 cycles durable macro-encapsulated aluminum with cavity by a sacrificial layer method for high temperature latent heat storage," *Chem. Eng. J.*, vol. 457, no. January, p. 141352, 2023, doi: 10.1016/j.cej.2023.141352.

[10] T. Kim, D. M. France, W. Yu, W. Zhao, and D. Singh, "Heat transfer analysis of a latent heat thermal energy storage system using graphite foam for concentrated solar power," *Sol. Energy*, vol. 103, pp. 438–447, 2014, doi: 10.1016/j.solener.2014.02.038.

[11] W. Zhao, D. M. France, W. Yu, T. Kim, and D. Singh, "Phase change material with graphite foam for applications in high-temperature latent heat storage systems of concentrated solar power plants," *Renew. Energy*, vol. 69, pp. 134–146, 2014, doi: 10.1016/j.renene.2014.03.031.

[12] D. Singh, T. Kim, W. Zhao, W. Yu, and D. M. France, "Development of graphite foam infiltrated with MgCl2 for a

latent heat based thermal energy storage (LHTES) system," *Renew. Energy*, vol. 94, pp. 660–667, 2016, doi: 10.1016/j.renene.2016.03.090.

[13] D. Singh, W. Yu, W. Zhao, T. Kim, D. M. France, and R. K. Smith, "Development and prototype testing of MgCl2/graphite foam latent heat thermal energy storage system," *Sol. Energy*, vol. 159, no. November 2017, pp. 270–282, 2018, doi: 10.1016/j.solener.2017.10.084.

[14] İ. G. Demirkıran, K. Niedermeier, and E. Çetkin, "Hollowed and perforated fins in latent heat storage units for High-Temperature hybrid thermal energy storage applications," *Energy Convers. Manag.*, vol. 340, no. April, 2025, doi: 10.1016/j.enconman.2025.119998.

[15] A. Alemam *et al.*, "Experimental demonstration of a dispatchable power-to-power high temperature latent heat storage system," *J. Energy Storage*, vol. 86, no. March, 2024, doi: 10.1016/j.est.2024.111241.

[16] J. P. Kotzé, T. W. Von Backström, and P. J. Erens, "Simulation and testing of a latent heat thermal energy storage unit with metallic phase change material," *Energy Procedia*, vol. 49, pp. 860–869, 2014, doi: 10.1016/j.egypro.2014.03.093.

[17] X. H. Yang, S. C. Tan, and J. Liu, "Numerical investigation of the phase change process of low melting point metal," *Int. J. Heat Mass Transf.*, vol. 100, pp. 899–907, 2016, doi: 10.1016/j.ijheatmasstransfer.2016.04.109.

[18] L. Shan, T. Nakamura, T. Nomura, A. Martin, and J. N. Chiu, "Single and cascaded high temperature latent heat thermal energy storage in concentrated solar power system: Case study," *Sol. Energy*, vol. 136, no. February, p. 118431, 2024, doi: 10.1016/j.est.2025.118431.

[19] S. Riahi, M. Evans, M. Belusko, M. Liu, and F. Bruno, "Orientation impact on structural integrity of a shell and tube latent heat thermal energy storage system," *J. Energy Storage*, vol. 52, no. PA, p. 104829, 2022, doi: 10.1016/j.est.2022.104829.

[20] K. Niedermeier, "A perspective on high-temperature heat storage using liquid metal as heat transfer fluid," *Energy Storage*, vol. 5, no. 8, pp. 1–12, 2023, doi: 10.1002/est2.530.

[21] M. A. Khuda, J. Khalesi, Z. Tu, Y. Long, D. Piccioni Koch, and N. Sarunac, "Numerical analysis of a developing turbulent flow and conjugate heat transfer for molten salt and liquid sodium in a solar receiver," *Appl. Therm. Eng.*, vol. 217, no. March, 2022, doi: 10.1016/j.applthermaleng.2022.119156.

[22] Z. G. Shen, S. Chen, and B. Chen, "Heat transfer performance of a finned shell-and-tube latent heat thermal energy storage unit in the presence of thermal radiation," *J. Energy Storage*, vol. 45, p. 103724, Jan. 2022, doi: 10.1016/J.EST.2021.103724.